



# Solid salt confinement effect: An effective strategy to fabricate high crystalline polymer carbon nitride for enhanced photocatalytic hydrogen evolution



Yangsen Xu<sup>a,b,1</sup>, Xin He<sup>c,1</sup>, Hong Zhong<sup>a</sup>, David J. Singh<sup>c,d</sup>, Lijun Zhang<sup>c,\*</sup>, Ruihu Wang<sup>a,\*</sup>

<sup>a</sup> State Key Laboratory of Structural Chemistry, Fujian Institute of Research on the Structure of Matter, Chinese Academy of Sciences, Fuzhou 350002, PR China

<sup>b</sup> International Collaborative Laboratory of 2D Materials for Optoelectronic Science & Technology, College of Optoelectronic Engineering, Shenzhen University, Shenzhen 518060, PR China

<sup>c</sup> Key Laboratory of Automobile Materials of MOE, State Key Laboratory of Superhard Materials, College of Materials Science and Engineering, Jilin University, Changchun 130012, PR China

<sup>d</sup> Department of Physics and Astronomy, University of Missouri, Columbia, MO, 65211-7010, USA

## ARTICLE INFO

### Keywords:

Crystalline polymer carbon nitride  
Water splitting  
Photocatalysis  
Template synthesis

## ABSTRACT

Polymer carbon nitrides (PCN) are one of promising photocatalysts in water splitting, but their low crystallinity usually leads to slow transfer efficiency of charge carriers. Herein, we presented a solid-salt-assisted growth strategy to fabricate highly crystalline polymer carbon nitride (CPCN). The high-melting-point KCl salt was used as an easily removable solid template, where the confined space guides efficient growth of CPCN. The fabricated CPCN samples show high crystalline quality with clear long-range periodicity and large grain sizes up to 400 nm. The combination of structural characterization analyses and first-principles energetic calculations reveals that CPCN is composed of chain-like melon motifs with intercalated K<sup>+</sup> ions. The photocatalytic activity of CPCN in hydrogen evolution reaction is over 22 times higher than that of pristine PCN, the apparent quantum efficiency at  $\lambda = 420 \pm 5$  nm is up to 11.4%. This work provides a simple and general protocol for crystallinity and performance enhancement in a wide range of polymeric photocatalyst materials.

## 1. Introduction

Photocatalytic water splitting for hydrogen production over semiconductor catalysts promises a clean and renewable energy source [1]. Key to this technology is the development of efficient and low-cost photocatalysts that function under visible light. As one type of metal-free photocatalysts for solar energy utilization, heptazine-based polymer carbon nitrides (PCN) have attracted intense interest due to their extraordinary chemical stability, facile preparation, visible light response and tunable electronic structure [2–7]. These characteristics have endowed PCN with great potentials in artificial photocatalysis [8–13]. Nevertheless, the photocatalytic activity over pristine PCN is limited by several inherent issues, such as low optical absorption threshold, high electron-hole recombination rate and sluggish surface reaction kinetics. Various strategies, such as element doping or vacancies [14–17], hybridization with other semiconductors [18–20] and nanostructure engineering [21–24] have been proposed to improve photocatalytic performance, but the efficiencies still do not meet

practical requirements under visible light irradiation. One of the major reasons is that PCN prepared by thermal-induced polymerization typically shows low crystallinity. The high-density defects serve as recombination centers of photogenerated electron-hole pair, thus leading to low transfer efficiency of charge carriers in water splitting reaction. It is highly desirable to develop a general and facile method to fabricate high-crystalline PCN for increasing their photocatalytic activities.

The template methods based on inorganic crystalline materials have been reported to be typical approaches for improving the crystallinity of PCN. One method is the use of Ni-foam as templates and catalysts, the structural defects caused by -NH<sub>2</sub> or -NH- groups could be reduced through the Ni-catalyzed dehydrogenation during the polymerization [25]. However, the Ni-foam needs to be removed through acid etching, the recovery and reuse of the sacrificial templates are a daunting challenge. The other method is the use of molten salts. Under the help of eutectic salts (e.g. KBr/LiBr, KCl/LiCl and NaCl/KCl/LiCl) with melting points below polymerization temperature of the precursors, the carbon nitrides with higher crystallinity than those obtained by

\* Corresponding author.

E-mail addresses: [lijun\\_zhang@jlu.edu.cn](mailto:lijun_zhang@jlu.edu.cn) (L. Zhang), [ruihu@fjirsm.ac.cn](mailto:ruihu@fjirsm.ac.cn) (R. Wang).

<sup>1</sup> Yangsen Xu and Xin He contributed equally to this work.

traditional polymerization have been achieved [26–32]. Furthermore, the intercalation of alkali metal ions in the carbon nitride materials shortens the interlayer distances owing to additional bonding schemes, the tighter packing of neighboring layers is favorable for improving light harvesting and accelerating the transfer of photogenerated carriers within the stacks. These PCN materials have exhibited distinct optoelectronic properties from amorphous PCNs and significantly enhanced photocatalytic activities under visible light irradiation [28,32–36]. However, these Li-containing molten salts are sensitive to H<sub>2</sub>O and CO<sub>2</sub>, the sample preparation is required to isolate from air. Although various structural models with or without incorporation of salt ions have been proposed to interpret the experimental observations [31,32,34,36–38], the role of the molten salts in affecting the crystallinity of PCN is still unclear. Thus, the exploration of an alternative route is urgently needed to overcome the issues associated with Li-containing molten salts and to reveal the mechanism underlying the crystallinity of PCN.

Herein, we present a solid-salt-assisted growth strategy to improve the crystallinity of PCN under an atmospheric environment. The solid salt with high melting point acts as an easily removable and recyclable template to guide the growth of crystalline polymer carbon nitride (CPCN). The fabricated CPCN samples have large grain sizes up to 400 nm and low-angle X-ray diffraction peaks clearly indicating long-range periodicity. We resolve the CPCN crystalline structure with the aid of first principles calculations to be a conjugation structure based on chain-like melon motifs with K<sup>+</sup> cations intercalated. The CPCN phases with high crystallinity show much enhanced photocatalytic performance for hydrogen evolution reaction than the PCN (by the factor of 22) under visible light illuminated. Our work provides a facile approach to enhance crystalline quality of PCN and other polymeric photocatalysts for photocatalytic activity improvement.

## 2. Experimental section

### 2.1. Preparation of CPCN sample

Melamine (3.0 g) and KCl (2.0 g) in EtOH (1 mL) were ground in an agate mortar. After dried at 65 °C for 0.5 h, the resultant mixture was heated to 550 °C at a rate of 3.3 °C min<sup>-1</sup> and kept at this temperature for 3 h in a tube furnace (inner diameter of 5 cm) with open two ends. The bright yellow-green product was obtained after cooled to room temperature, washed with a copious of boiling deionized water and dried at 60 °C under vacuum. PCN was obtained using the same procedures as that of CPCN except KCl.

### 2.2. Photocatalytic activity test

Photocatalytic water splitting reactions were carried out in a 150 mL Pyrex flask reactor (Labsolar IIIAG, Perfectlight Technology Co., Ltd., Beijing, China) via top irradiation connected to a closed gas-evacuation and circulation system. Hydrogen production was performed by dispersing 50 mg of the catalyst powder in an aqueous solution (50 mL) containing 5 mL of 10 vol% triethanolamine (TEOA) as a sacrificial agent. 1.0 wt% Pt was loaded on the surface of the photocatalyst as a cocatalyst using an *in situ* photodeposition method with H<sub>2</sub>PtCl<sub>6</sub> under visible light ( $\lambda \geq 420$  nm). The reaction solution was evacuated several times to completely remove the air prior to irradiation under a 300 W Xe lamp. The wavelength of the incident light was controlled by applying the appropriate long-pass cutoff filters. The temperature of the reaction solution was maintained at 5 °C using a thermostatic water bath during the reaction. The amount of evolved gas was determined online using a gas chromatograph (Fuli 9790II, Zhejiang) with a TCD detector.

## 3. Results and discussion

The synthetic route of CPCN is schematically depicted in Fig. 1a.

Melamine was firstly ground with KCl in the presence of small amount of ethanol to form a homogeneous mixture, subsequent thermal polymerization at 550 °C under an atmospheric environment gave rise to KCl@CPCN. After thoroughly washed with deionized water to remove KCl, CPCN was obtained as a bright yellow powder. It should be mentioned that solid KCl possesses a melting point of 770 °C, which is higher than polymerization temperature of melamine. It acts as a solid template to provide an inter-crystal confined space to effectively guide the growth of high-quality CPCN. KCl could be easily isolated from KCl@CPCN and recovered for further use in the synthesis of CPCN. As a comparison, PCN was prepared under the identical conditions in the absence of KCl.

The N<sub>2</sub> adsorption-desorption experiments at 77 K show that Brunauer-Emmett-Teller (BET) specific surface area of PCN and CPCN are 25.3 and 13.5 m<sup>2</sup> g<sup>-1</sup>, respectively (Fig. S1). The elemental analyses show that the atomic ratios of C:N in PCN and CPCN are 0.61 and 0.64, respectively, both of them are close to that of melon (0.67). The content of element K in CPCN is 9.5 wt%, as determined by inductively coupled plasma (ICP) analysis. These results have validated a structure consisting of a melon-based framework with intercalated K<sup>+</sup> ions. X-ray diffraction (XRD) measurements indicate high crystallinity of CPCN (Fig. 1b). The XRD pattern of PCN presents two typical diffraction peaks at 27.50 and 13.02°, which are assigned to the (002) and (100) crystal facets, respectively. They represent the interplanar stacking of carbon nitride layers and in-plane repeating units of the continuous heptazine framework, respectively [39,40]. In comparison with PCN, it is obvious that the main diffraction peak of the (002) facet shifts from 27.50 to 28.36°, which suggests the narrowing of the interlayer distances from 0.324 to 0.315 nm owing to the intercalation of K<sup>+</sup> ions in CPCN (Fig. 1d), which is conducive to promoting polarization and charge transfer among the neighboring layers. In addition, the peak becomes sharp and narrow, indicative of higher crystallinity in CPCN. Thus, the template effects of solid KCl could guide the ordered growth of carbon nitrides in the confined space among KCl crystals during thermal polymerization of melamine (Fig. 1a). Particularly, the weak low-angle reflection peak at 13.02° disappears in CPCN. Instead, two new peaks occur at 8.015 and 9.915°, which correspond to the crystal lattice distances about 1.103 and 0.892 nm, respectively. It should be mentioned that the XRD pattern of CPCN is different from those obtained using KCl/LiCl as templates [29,31,32]. These observations have demonstrated the critical role of KCl salt in the growth of CPCN. The effects of KCl loading in the precursors on the evolution from PCN to CPCN are further investigated. As shown in Fig. S2, when the loading of KCl is less than 0.5 g in 3.0 g melamine, the characteristic (002) diffraction peak shifts toward high 2θ angle as increasing KCl loading, the gradual shift in their XRD patterns show that low content of KCl could not supply enough confined space for the oriented growth of CPCN. When the loading of KCl is more than 0.5 g, the characteristic diffraction peaks of CPCN are observed and the (002) peak gradually sharpens. After the usage of 2.0 g KCl for 3.0 g melamine, further increasing KCl loading in the precursor has no appreciable effect on the peak positions and intensities. Impressively, CPCN also could be expediently fabricated either using the recovered KCl or under nitrogen atmosphere, as validated by their identical XRD patterns (Fig. S3). This recycled solid-salt template process is completely different with the reported disposable molten-salt methods [31,32,34,36–38]. More details about the differences on sample quality and photocatalytic performance between this solid-salt process and the molten-salt methods are given in Table S1. These results demonstrated that our synthetic strategy is facile and cost-effective for fabricating high-crystalline carbon nitride materials.

The critical role of KCl salt in the crystallinity enhancement was further clarified by resolving structure of CPCN. By combining the information obtained from XRD patterns and comprehensive first-principles total energy minimization calculations of the candidate structures, the chemical composition of CPCN could be defined as C<sub>12</sub>N<sub>18</sub>H<sub>6</sub>K, and the unit cell of the theoretically optimized structure is

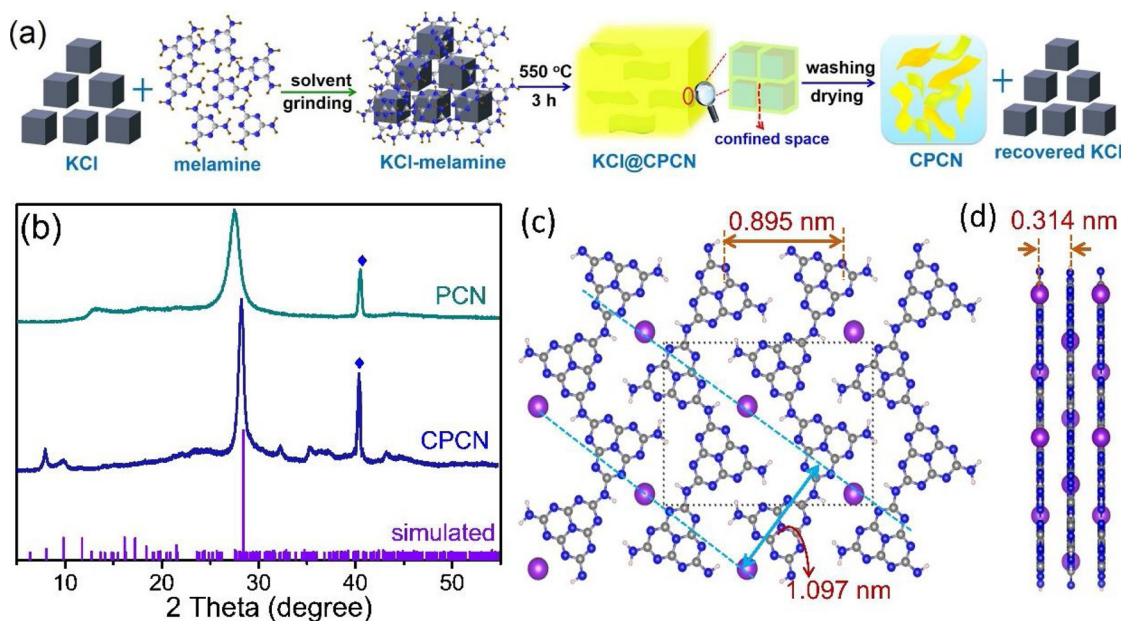


**Fig. 1.** (a) Schematic illustration of solid salt confinement strategy for the preparation of CPCN. (b) XRD patterns of CPCN and PCN. The purple vertical lines represent the simulated results using the resolved structure of CPCN. The symbol ◆ represents the Bragg peak of Mo (110) (JCPDS 42-1120), which acts as an internal reference to correct the intrinsic diffraction peak of the synthesized materials. (c) Top and (d) side views of the resolved structure of CPCN. The elements of C, N and K are in gray, blue and purple, respectively (For interpretation of the references to colour in this figure legend, the reader is referred to the web version of this article).

**Table 1**

The experimental and calculated data for the crystal structure of CPCN. The experimental data for PCN are also given for comparison.

	Experimental data			Calculated data				
	2 theta	d (nm)	FWHM	h	k	l	2-theta	d (nm)
CPCN	8.015	1.103	0.33	1	0	0	6.367	1.387
	9.915	0.892	—	1	1	0	8.056	1.097
	11.62	0.761	—	0	2	0	9.869	0.896
	16.12	0.550	—	1	2	0	11.75	0.752
	28.36	0.315	0.55	1	3	0	16.15	0.548
	32.38	0.276	—	0	2	1	17.23	0.514
	43.35	0.209	—	1	2	1	18.36	0.482
	13.02	0.680	—	2	2	1	21.49	0.413
PCN	27.50	0.324	1.07	0	0	2	28.40	0.314

$a = 13.87 \text{ \AA}$ ,  $b = 17.91 \text{ \AA}$  and  $c = 6.28 \text{ \AA}$ . The structure consists of one-dimensional amine-linked heptazine-based melon chains, in which  $\text{K}^+$  ions are intercalated in the interstitial region (Fig. 1c). The neighboring polymeric chains are extended into two-dimensional supramolecular arrays through hydrogen bonds. The simulated XRD pattern is in a reasonable agreement with the experimental data of as-synthesized CPCN. According to the simulated XRD results, the main visible peaks at 8.015, 9.915, 11.62 and 28.36° are assigned to the (110), (020), (120) and (002) crystal facets, respectively (Table 1). More details about the crystal facets are listed in Table S2. The high crystallinity of CPCN is further indicated by the semi-quantitative index based on the full width at half maximum (FWHM) of XRD peaks. Smaller FWHM corresponds to higher crystallinity. As shown in Table 1, CPCN has a small FWHM (0.55) for the strongest diffraction peak, which is nearly two times lower than that of PCN (1.07).

Transmission electron microscopy (TEM) images were taken to discern the morphologies of CPCN and PCN. As shown in Fig. 2a, PCN is an amorphous aggregate on the microscale, while CPCN shows multiple separated sheets on the nanoscale with the grain size up to  $0.5 \mu\text{m}$  (Fig. S4). The nanosheet feature of CPCN is probably attributed to the confinement effect of KCl and the interaction of  $\text{K}^+$  ions, leading to effective exfoliation of bulk CPCN (Fig. 2b), which is conducive to

enhancing photocatalytic activity in water splitting. In sharp contrast with the selected area electron diffraction (SAED) pattern of PCN, the bright spots are detected in the SAED pattern of CPCN (Fig. 2c). The spots in the center rings of CPCN provide the lattice distances of approximately 1.099 (marked in red) and 0.901 nm (marked in yellow), corresponding to the (110) and (020) facets, respectively. Other spots with lattice distance of 0.313 nm (marked by cyan cycles) are assigned to the (002) facet, corresponding to the interlayer separation between CPCN nanosheets. The clear lattice fringes in high-resolution TEM further validate high crystallinity of CPCN, and the lattice distance about 0.446 nm is indexed to (040) facet (Fig. 2d). These TEM analyses are well consistent with the results of XRD patterns and theoretical calculations.

Fourier transform infrared (FTIR), solid-state  $^{13}\text{C}$  NMR, X-ray photoelectron spectroscopy (XPS) and near edge X-ray absorption fine structure (NEXAFS) spectra were performed to characterize the structure of CPCN. In the FTIR spectra of PCN and CPCN (Fig. 3a and Fig. S5), the peak at  $809 \text{ cm}^{-1}$  corresponds to the out-of-plane bending of the heptazine rings, while the fingerprint peaks at  $1200\text{--}1700 \text{ cm}^{-1}$  represent the stretching and bending modes of the conjugated heterocycles. Besides, CPCN shows two new bands at  $2180$  and  $2148 \text{ cm}^{-1}$ , which are assigned to the stretching vibration of cyano groups ( $\text{C}\equiv\text{N}$ ), probably stemming from the decomposition or incomplete polymerization of heptazine units. [28,41] Notably, the FTIR spectrum of CPCN obtained under nitrogen atmosphere is identical with that of as-synthesized CPCN, which shows that these new bands are not associated with oxygen-containing groups but with the  $\text{C}\equiv\text{N}$  stretching vibration [36]. The characteristic peak of the  $\text{C}-\text{N}$  vibration occurs at  $889 \text{ cm}^{-1}$  in PCN, while two new peaks occur at  $993$  and  $914 \text{ cm}^{-1}$  in CPCN owing to the incorporation of  $\text{K}^+$  ions and the presence of electron-withdrawing  $-\text{C}\equiv\text{N}$  group. These characteristics also break the balance of vibration of  $\text{N}-\text{H}$ , leading to the emergence of new peaks at  $1114$  and  $1150 \text{ cm}^{-1}$  in CPCN. Meantime, they also induce downfield shift of the resonance peaks in the solid-state  $^{13}\text{C}$  NMR spectrum of CPCN when compared with that in PCN (Fig. 3b). It should be mentioned that these resonance peaks are similar to those in melem/melon, but different from that of triazine-based melon, [32,42] clearly confirming the presence of heptazine-based skeleton in both PCN and

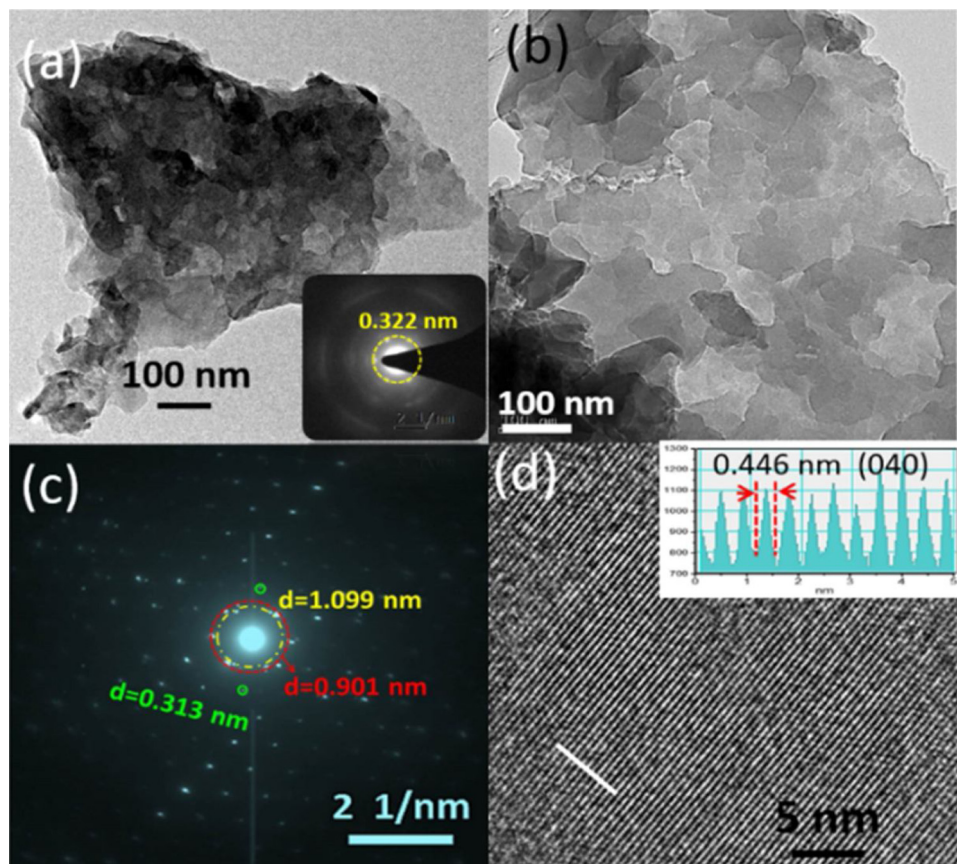


**Fig. 2.** TEM images for (a) PCN and (b) CPCN. (c) The SAED pattern for CPCN. (d) HRTEM image for CPCN. The inset in (a) is the SAED pattern of PCN, and the inset in (d) is the lattice fringes of CPCN along the white line.

CPCN.

XPS survey spectrum of CPCN shows the presence of K, C, N, O and Cl (Fig. S6), while there is only C, N and O in XPS survey spectrum of PCN, which reveals the incorporation of  $K^+$  in CPCN. The chemical state of K in CPCN was verified by high-resolution K 2p XPS analyses (Fig. 3c). Two binding energy peaks at 292.9 and 295.7 eV are

correlated with those of K 2p in  $CH_3CH_2OCOOK$  [43] and are distinct from those for metallic K (294.7 eV). The doublet separation of the K 2p photoelectron line is 2.8 eV, further validating that K in CPCN is  $K^+$  ion. The deconvolution of C 1s XPS spectrum in CPCN provides three binding energy peaks at 284.8, 286.4 and 288.1 eV. The peaks at 288.1 and 284.8 eV are similar to those in PCN, corresponding to  $sp^2$ -

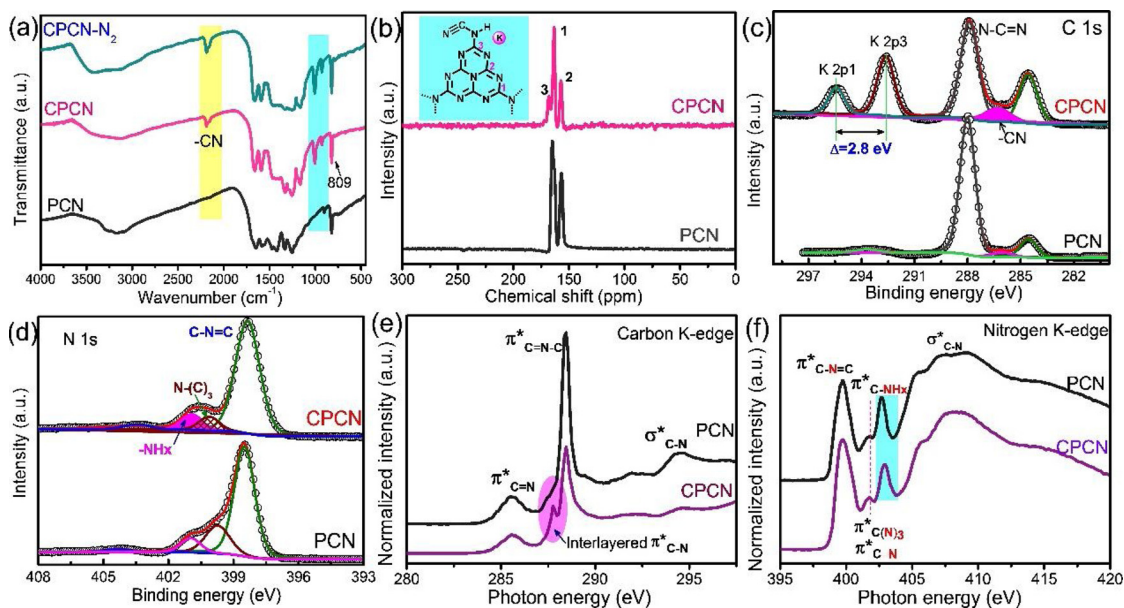


**Fig. 3.** (a) FTIR spectra for PCN and CPCN synthesized in air and  $N_2$ . (b) Solid-state  $^{13}C$  NMR spectra of PCN and CPCN, the inset is the proposed structure of CPCN. (c) High-resolution K 2p and C 1s XPS spectra and (d) N 1s XPS spectra for PCN and CPCN. (e) Carbon and (f) nitrogen K-edge NEXAFS spectra of PCN and CPCN.

hybridized carbon atoms in aromatic N=C=N species [44] and graphitic carbon or adventitious carbon contamination, respectively. The weak binding energy peak at 286.4 eV in CPCN probably originates from cyano group [45], which is agreement with the FTIR result. High-resolution N 1 s XPS spectra in both PCN and CPCN show three binding energy peaks (Fig. 3d). The strongest peak at 398.5 eV is assigned to the nitrogen atoms of C=N=C in the heptazine units, which is viewed as the primary building units in the conjugated structure. Other peaks at 400.0 and 400.9 eV correspond to the tertiary nitrogen N-(C)<sub>3</sub> and the bridging –NH– or terminal amino groups, respectively [46]. The chemical structure of as-synthesized CPCN was further probed by NEXAFS. In the carbon K-edge NEXAFS spectra (Fig. 3e), both PCN and CPCN show the characteristic resonances of  $\pi^*_{\text{C}=\text{N}}$  at 285.6 eV and  $\pi^*_{\text{C}-\text{N}=\text{C}}$  at 288.5 eV in heptazine rings. A sharp shoulder peak corresponding to the  $\pi^*_{\text{C}=\text{N}-\text{C}}$  species appears at 287.8 eV in CPCN, which is ascribed to the out-of-plane orientation in CPCN for the increased interlayer interaction, [47] which is line with the narrowed interlayer distance as elucidated by XRD analyses. The nitrogen K-edge NEXAFS spectrum of CPCN shows two typical  $\pi^*$  resonance peaks at 399.7 and 402.6 eV (Fig. 3f), which are assigned to aromatic C=N=C and -NH- bridging species, respectively. [47] The  $\pi^*$  resonance peak at 401.6 eV is attributed to the tertiary nitrogen N-(C)<sub>3</sub> and cyano groups [48].

The high crystallinity and K<sup>+</sup> incorporation endow CPCN with attractive photoelectronic properties. In the UV-vis diffuse reflectance spectra (Fig. 4a), CPCN shows a wide and sharp light absorption threshold at 460 nm, an obvious redshift is observed when compared with that of PCN at 420 nm. The optical band gaps determined from the transformed Kubelka-Munk function for CPCN and PCN are 2.71 and 2.78 eV, respectively (Fig. S7). The XPS valence-band analyses (inset of Fig. 4a) indicate that the valence-band potential of CPCN is 1.91 eV, which is 0.07 eV higher than that of 1.98 eV in PCN, indicating that the electronic structure of CPCN is changed. A schematic illustration of the band structures of CPCN and PCN was shown in Fig. 4b, both CPCN and PCN have the same conduction band potential (-0.8 eV vs NHE, pH = 7). In addition to enhanced visible-light absorption efficiency, CPCN is more effective in promoting separation of the photoexcited charge carriers, as confirmed by the steady-state photoluminescence spectra (Fig. 4c). The weak emission peak centered at 465 nm suggests a low radiative recombination rate and efficient separation of photo-

excited carriers in CPCN. To further confirm the transfer efficiency of photo-generated charge carriers, time-resolved transient fluorescence decay spectroscopy was performed (Fig. 4d). The average lifetime of the fluorescence decay in CPCN is 0.53 ns, which is much shorter than that of 2.28 ns in PCN (Table S3.). The decreased lifetime suggests the exciton dissociation due to the shortened interlayer distance and high crystallinity in CPCN [7,49,50], which are favorable for accelerating charge transfer from the interlayers to the interface/surface without recombination.

To assess the validity of high crystallinity and K<sup>+</sup> incorporation on improving photocatalytic efficiency, the visible-light-induced hydrogen evolution assays for CPCN and PCN were carried out. As shown in Fig. 4e, CPCN exhibits significantly enhanced photocatalytic activity in hydrogen evolution reaction when compared with PCN. The initial H<sub>2</sub> evolution rate over CPCN reaches 1356 μmol h<sup>-1</sup> g<sup>-1</sup>, which is 22 times higher than that of 60 μmol h<sup>-1</sup> g<sup>-1</sup> in PCN. TEM images show that Pt nanoparticles were *in situ* formed after photocatalytic reaction, they are immobilized on PCN and CPCN and are similar to each other (Fig. S8). The stability of CPCN was examined by repeatedly conducting hydrogen evolution reaction under visible light irradiation. The photocatalytic activities have no significant variation after consecutive operation for five cycles (Fig. 4e). The TEM images and XRD results show the structure and morphology are well maintained in recovered CPCN (Fig. S9). Notably, the suspended CPCN in water shows an appreciable color change during hydrogen evolution reaction. As shown in Fig. 4f, yellow CPCN gradually turns into blue color, which could be held during photocatalytic reaction. After removing away light source, the color of CPCN returns to yellow color. The process could be repeated under visible light irradiation. In sharp comparison, there is no color change in the PCN photocatalytic system. The switchable color change in CPCN probably originates from the electron accumulation [6,51,52] in the presence of TEOA during water splitting, which not only guarantees the dissociation of excitons to generate adequate hot carriers, but also improves the separation of electron-hole pairs, thus resulting in high photocatalytic activity.

To unravel the photocatalytic mechanism of CPCN, density functional theory (DFT) calculations based on the electronic structure were performed. The dispersive van der Waals interaction that cannot be ignored in layered PCN/CPCN is included. As shown in Fig. 5a and Fig.

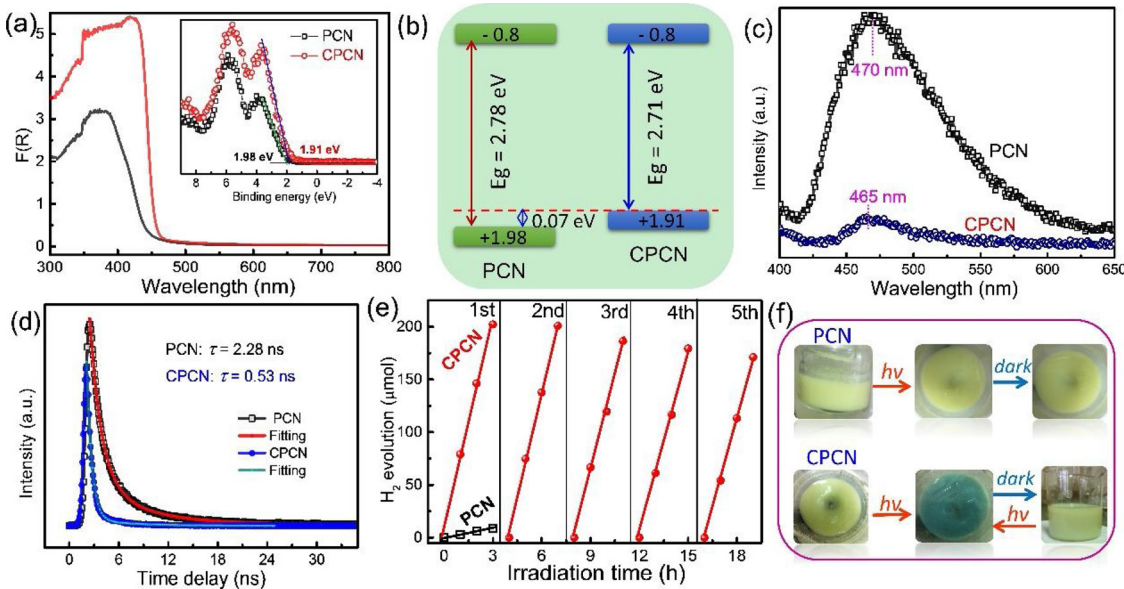
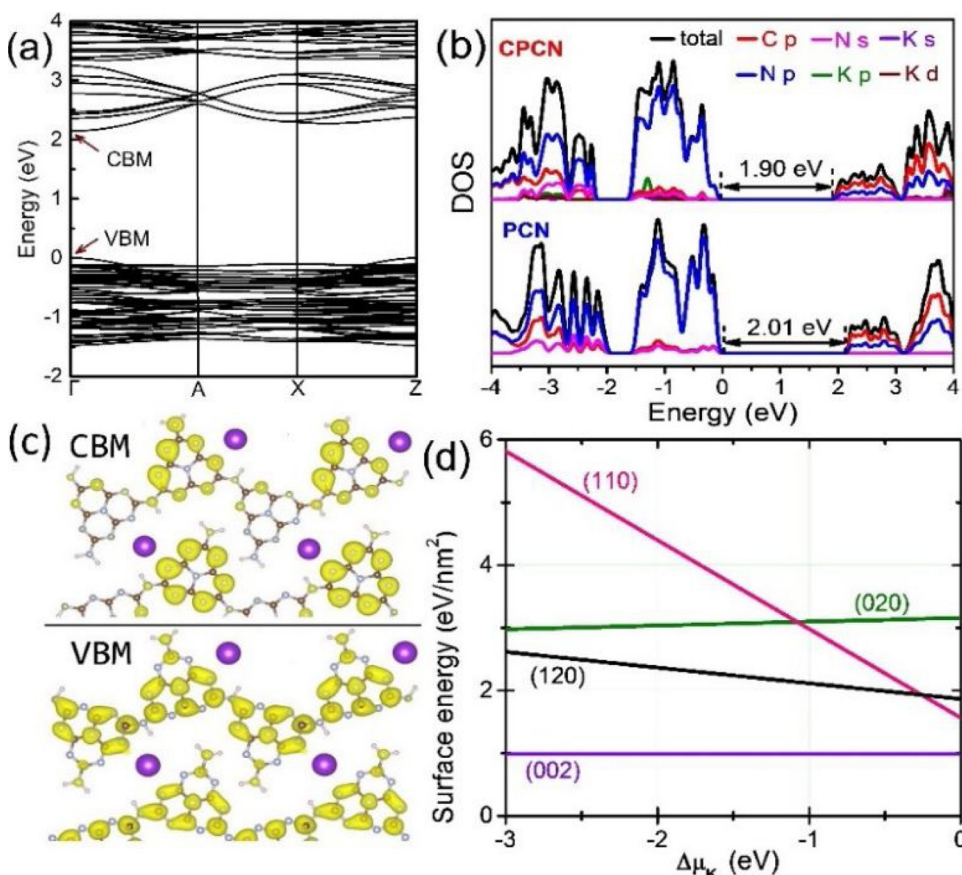


**Fig. 4.** (a) UV-vis diffuse reflectance spectra of PCN and CPCN, the inset is the corresponding XPS valence-band spectra. (b) Schematic diagram of the electronic band alignment, (c) the steady-state photoluminescence spectra and (d) the time-resolved fluorescence decay spectra for PCN and CPCN. (e) Hydrogen evolution reaction for PCN and CPCN under visible light irradiation ( $420 \text{ nm} \leq \lambda \leq 780 \text{ nm}$ ) at 5 °C. (f) Digital photos of PCN and CPCN suspensions in water before and after visible light irradiation.



S10). The band gap difference (0.11 eV) between CPCN and PCN is similar to the experimental result (0.07 eV), although the gap magnitudes are smaller than the experimental values owing to known self-interaction error in standard DFT calculations. The higher-level hybrid functional calculations [53] for PCN and CPCN give larger band gaps of 3.1 and 2.8 eV, respectively, which are in better accord with the experimental results. Notably, the band gap difference shows the same trend as that of standard DFT calculations. For both PCN and CPCN, the valence-band maximum (VBM) consists mainly of N-p states, and the conduction-band minimum (CBM) is predominated by the hybridization between N-p and C-p states (Fig. 5b). The K<sup>+</sup> ions intercalated in CPCN do not directly participate in the formation of the electronic states at band edges, but their existence has exerted a non-negligible effect on the electronic behavior. As shown in the band-decomposed charge densities of VBM and CBM in CPCN (Fig. 5c), the VBM state is distributed uniformly throughout the C–N framework with chain-like melon motifs, while the CBM state is located in local region closer to K<sup>+</sup>. The behavior is different from the case in PCN, where both the CBM and VBM states show uniform distribution (Fig. S11). The (110), (020) and (120) exposed facets show much higher surface energy than the (002) facet (Fig. 5d), as expected from the creation of dangling bonds at the cleavage surface. These relatively high-surface-energy exposed facets could be found in the experimental XRD pattern of CPCN (Table 1), revealing that they have been formed in the solid-salt-assistant confinement growth process, which contributes to increasing photocatalytic activity of CPCN.

#### 4. Conclusion

A solid-salt-assisted growth strategy has been developed to fabricate high-crystalline polymer carbon nitrides. The remarkably enhanced activity has been validated to originate from high crystallinity of CPCN and shortened interlayer distance, which broaden light harvesting and

**Fig. 5.** (a) Electronic band structure of CPCN. (b) The total and atomic-orbital projected density of states for CPCN and PCN. (c) The band-decomposed charge densities of VBM and CBM for CPCN obtained using DFT calculations with the PBE functional. (d) Calculated surface energies of the (110), (020), (120) and (002) crystal facets in CPCN.

promote the transfer of photogenerated carriers. Importantly, CPCN could be fabricated under an atmospheric environment using KCl as a structure-directing template. Unlike conventional inorganic oxide hard templates, the water-soluble KCl is easily extracted from the product, and the recovered KCl could be reused for the consecutive synthesis of CPCN. In summary, this work presents a facile, environment-benign and cost-effective approach towards large-scale production of high-performance polymer carbon nitrides and other polymeric photocatalysts. Further investigation for the effects of other solid salts on the crystallinity of carbon nitrides and photocatalytic performance are on progress.

#### Acknowledgements

This work was financially supported by the National Natural Science Foundation of China (21401190, 61722403 and 11674121), Natural Science Foundation of Fujian Province (2017J05035) and Strategic Priority Research Program of the Chinese Academy of Sciences (XDB20000000). NEXAFS experiments were performed at the Catalysis and Surface Science Endstation in the National Synchrotron Radiation Laboratory (NSRL) in Hefei, China.

#### Appendix A. Supplementary data

Supplementary material related to this article can be found, in the online version, at doi:<https://doi.org/10.1016/j.apcatb.2019.01.069>.

#### References

- [1] J. Qi, W. Zhang, R. Cao, *Adv. Energy Mater.* 8 (2018) 1701620.
- [2] X.C. Wang, K. Maeda, A. Thomas, K. Takanabe, G. Xin, J.M. Carlsson, K. Domen, M. Antonietti, *Nat. Mater.* 8 (2009) 76–80.
- [3] W.J. Ong, L.L. Tan, Y.H. Ng, S.T. Yong, S.P. Chai, *Chem. Rev.* 116 (2016) 7159–7329.

- [4] H. Kasap, C.A. Caputo, B.C.M. Martindale, R. Godin, V.W.H. Lau, B.V. Lotsch, J.R. Durrant, E. Reisner, *J. Am. Chem. Soc.* 138 (2016) 9183–9192.
- [5] J.J. Ji, J. Wen, Y.F. Shen, Y.Q. Lv, Y.L. Chen, S.Q. Liu, H.B. Ma, Y.J. Zhang, *J. Am. Chem. Soc.* 139 (2017) 11698–11701.
- [6] V.W.H. Lau, D. Klose, H. Kasap, F. Podjaski, M.C. Pignie, E. Reisner, G. Jeschke, B.V. Lotsch, *Angew. Chemie Int. Ed.* 56 (2017) 510–514.
- [7] G.G. Zhang, G.S. Li, Z.A. Lan, L.H. Lin, A. Savateev, T. Heil, S. Zafeiratos, X.C. Wang, M. Antonietti, *Angew. Chemie Int. Ed.* 56 (2017) 13445–13449.
- [8] A. Savateev, I. Ghosh, B. Konig, M. Antonietti, *Angew. Chemie Int. Ed.* 57 (2018) 15936–15947.
- [9] B. Kurpil, B. Kumru, T. Heil, M. Antonietti, A. Savateev, *Green Chem.* 20 (2018) 838–842.
- [10] W.G. Tu, Y. Zhou, Z.G. Zou, *Adv. Mater.* 26 (2014) 4607–4626.
- [11] B. Kurpil, K. Otte, M. Antonietti, A. Savateev, *Appl. Catal. B Environ.* 228 (2018) 97–102.
- [12] C.T. Qiu, Y.S. Xu, X. Fan, D. Xu, R. Tandiana, X. Ling, Y. Jiang, C. Liu, L. Yu, W. Chen, C.L. Su, *Adv. Sci.* 6 (2019) 1801403.
- [13] A. Savateev, M. Antonietti, *ACS Catal.* 8 (2018) 9790–9808.
- [14] S.E. Guo, Z.P. Deng, M.X. Li, B.J. Jiang, C.G. Tian, Q.J. Pan, H.G. Fu, *Angew. Chemie Int. Ed.* 55 (2016) 1830–1834.
- [15] J.S. Zhang, J.H. Sun, K. Maeda, K. Domen, P. Liu, M. Antonietti, X.Z. Fu, X.C. Wang, *Energy Environ. Sci.* 4 (2011) 675–678.
- [16] S.A. Shevlin, Z.X. Guo, *Chem. Mater.* 28 (2016) 7250–7256.
- [17] W.G. Tu, Y. Xu, J.J. Wang, B.W. Zhang, T.H. Zhou, S.M. Yin, S.Y. Wu, C.M. Li, Y.Z. Huang, Y. Zhou, Z.G. Zou, J. Robertson, M. Kraft, R. Xu, *ACS Sustain. Chem. Eng.* 5 (2017) 7260–7268.
- [18] Y.S. Xu, W.D. Zhang, *ChemCatChem* 5 (2013) 2343–2351.
- [19] F. He, G. Chen, J.W. Miao, Z.X. Wang, D. Su, S. Liu, W.Z. Cai, L.P. Zhang, S. Hao, B. Liu, *ACS Energy Lett.* 1 (2016) 969–975.
- [20] Y.S. Xu, L.P. Li, C.T. Qiu, X.S. Huang, G.S. Li, *ChemistrySelect* 4 (2019) 190–195.
- [21] P. Niu, M. Qiao, Y.F. Li, L. Huang, T.Y. Zhai, *Nano Energy* 44 (2018) 73–81.
- [22] Z.X. Zhou, Y.Y. Zhang, Y.F. Shen, S.Q. Liu, Y.J. Zhang, *Chem. Soc. Rev.* 47 (2018) 2298–2321.
- [23] L.F. Cui, J.L. Song, A.F. McGuire, S.F. Kang, X.Y. Fang, J.J. Wang, C.C. Yin, X. Li, Y.G. Wang, B.X. Cui, *ACS Nano* 12 (2018) 5551–5558.
- [24] M. Wu, J. Zhang, B.B. He, H.W. Wang, R. Wang, Y.S. Gong, *Appl. Catal. B Environ.* 241 (2019) 159–166.
- [25] W.N. Xing, W.G. Tu, Z.H. Han, Y.D. Hu, Q.Q. Meng, G. Chen, *ACS Energy Lett.* 3 (2018) 514–519.
- [26] M.J. Bojdys, J.O. Muller, M. Antonietti, A. Thomas, *Chem. Eur. J.* 14 (2008) 8177–8182.
- [27] G. Algarra-Siller, N. Severin, S.Y. Chong, T. Bjorkman, R.G. Palgrave, A. Laybourn, M. Antonietti, Y.Z. Khimyak, A.V. Krasheninnikov, J.P. Rabe, U. Kaiser, A.I. Cooper, A. Thomas, M.J. Bojdys, *Angew. Chem. Int. Ed.* 53 (2014) 7450–7455.
- [28] K. Schwinghammer, B. Tuffy, M.B. Mesch, E. Wirthner, C. Martineau, F. Taulelle, W. Schnick, J. Senker, B.V. Lotsch, *Angew. Chem. Int. Ed.* 52 (2013) 2435–2439.
- [29] L.H. Lin, C. Wang, W. Ren, H.H. Ou, Y.F. Zhang, X.C. Wang, *Chem. Sci.* 8 (2017) 5506–5511.
- [30] A. Savateev, D. Dontsova, B. Kurpil, M. Antonietti, *J. Catal.* 350 (2017) 203–211.
- [31] A. Savateev, S. Pronkin, J.D. Epping, M.G. Willinger, C. Wolff, D. Neher, M. Antonietti, D. Dontsova, *ChemCatChem* 9 (2017) 167–174.
- [32] L.H. Lin, H.H. Ou, Y.F. Zhang, X.C. Wang, *ACS Catal.* 6 (2016) 3921–3931.
- [33] Z.X. Zeng, H.T. Yu, X. Quan, S. Chen, S.S. Zhang, *Appl. Catal. B Environ.* 227 (2018) 153–160.
- [34] K. Schwinghammer, M.B. Mesch, V. Duppel, C. Ziegler, J. Senker, B.V. Lotsch, *J. Am. Chem. Soc.* 136 (2014) 1730–1733.
- [35] C.J. Pickard, A. Salamat, M.J. Bojdys, R.J. Needs, P.F. McMillan, *Phys. Rev. B* 94 (2016) 094104–094110.
- [36] V.W.H. Lau, I. Moudrakovski, T. Botari, S. Weinberger, M.B. Mesch, V. Duppel, J. Senker, V. Blum, B.V. Lotsch, *Nat. Commun.* 7 (2016) 12165–12174.
- [37] H.L. Gao, S.C. Yan, J.J. Wang, Y.A. Huang, P. Wang, Z.S. Li, Z.G. Zou, *Phys. Chem. Chem. Phys.* 15 (2013) 18077–18084.
- [38] D. Dontsova, S. Pronkin, M. Wehle, Z.P. Chen, C. Fettkenhauer, G. Clavel, M. Antonietti, *Chem. Mater.* 27 (2015) 5170–5179.
- [39] J.R. Ran, T.Y. Ma, G.P. Gao, X.W. Du, S.Z. Qiao, *Energy Environ. Sci.* 8 (2015) 3708–3717.
- [40] F.K. Kessler, Y. Zheng, D. Schwarz, C. Merschjann, W. Schnick, X.C. Wang, M.J. Bojdys, *Nat. Rev. Mater.* 2 (2017) 17030.
- [41] Y.P. Wang, Y.K. Li, W. Ju, J.C. Wang, H.C. Yao, L. Zhang, J.S. Wang, Z.J. Li, *Carbon* 102 (2016) 477–486.
- [42] J.R. Holst, E.G. Gillan, *J. Am. Chem. Soc.* 130 (2008) 7373–7379.
- [43] A. Ihss, K. Uvdal, B. Liedberg, *Langmuir* 9 (1993) 733–739.
- [44] L. Sun, M.J. Yang, J.F. Huang, D.S. Yu, W. Hong, X.D. Chen, *Adv. Funct. Mater.* 26 (2016) 4943–4950.
- [45] L.H. Lin, W. Ren, C. Wang, A.M. Asiri, J. Zhang, X.C. Wang, *Appl. Catal. B Environ.* 231 (2018) 234–241.
- [46] J.J. Chen, Z.Y. Mao, L.X. Zhang, D.J. Wang, R. Xu, L.J. Bie, B.D. Fahlman, *ACS Nano* 11 (2017) 12650–12657.
- [47] Y. Zheng, Y. Jiao, Y.H. Zhu, L.H. Li, Y. Han, Y. Chen, A.J. Du, M. Jaroniec, S.Z. Qiao, *Nat. Commun.* 5 (2014) 3783.
- [48] I. Shimoyama, G.H. Wu, T. Sekiguchi, Y. Baba, *Phys. Rev. B* 62 (2000) R6053–R6056.
- [49] H. Wang, S.L. Jiang, S.C. Chen, X.D. Zhang, W. Shao, X.S. Sun, Z. Zhao, Q. Zhang, Y. Luo, Y. Xie, *Chem. Sci.* 8 (2017) 4087–4092.
- [50] H. Wang, X.S. Sun, D.D. Li, X.D. Zhang, S.C. Chen, W. Shao, Y.P. Tian, Y. Xie, *J. Am. Chem. Soc.* 139 (2017) 2468–2473.
- [51] Z.X. Zeng, X. Quan, H.T. Yu, S. Chen, Y.B. Zhang, H.M. Zhao, S.S. Zhang, *Appl. Catal. B Environ.* 236 (2018) 99–106.
- [52] A. Savateev, B. Kurpil, A. Mishchenko, G.G. Zhang, M. Antonietti, *Chem. Sci.* 9 (2018) 3584–3591.
- [53] A.V. Kruckau, O.A. Vydrov, A.F. Izmaylov, G.E. Scuseria, *J. Chem. Phys.* 125 (2006) 224106.